Numerical analysis of indentation-induced cracking of brittle coatings on ductile substrates

Abdul-Baqi, A.; van der Giessen, E.

Published in:
International Journal of Solids and Structures

DOI:
10.1016/S0020-7683(01)00280-3

Publication date:
2002

PERGAMON

International Journal of Solids and Structures 39 (2002) 1427–1442

INTERNATIONAL JOURNAL OF SOLIDS and STRUCTURES

www.elsevier.com/locate/ijsolstr

Numerical analysis of indentation-induced cracking of brittle coatings on ductile substrates

A. Abdul-Baqi [a], E. Van der Giessen [b,*]

[a] *Delft University of Technology, Koiter Institute Delft, Mekelweg 2, 2628 CD Delft, Netherlands*
[b] *University of Groningen, Department of Applied Physics, Nyenborgh 4, 9747 AG Groningen, Netherlands*

Received 15 August 2001; received in revised form 7 November 2001

Abstract

Cracking of hard coatings during indentation is studied using the finite element method. The coating is assumed to be linear elastic, the substrate is elastic-perfectly plastic and the indenter is spherical and rigid. Through-thickness cracks are modeled using cohesive surfaces, with a finite strength and fracture energy. The interface between the coating and the substrate is also modeled by means of cohesive zones but with interface properties. The primary potential locations for the initiation of coating cracks are the coating surface close to the contact edge and the coating side of the interface in the contact region, where high values of tensile radial stress are found. Circumferential cracks are found to initiate from the coating surface and to propagate towards the interface. The initiation and advance of a crack is imprinted on the load–displacement curve as a kink. The spacing between successive cracks is found to be of the order of the coating thickness. The influence of other material and cohesive parameters on the initiation of the first crack and spacing between successive cracks is also investigated.

Keywords: Indentation; Fracture; Coatings; Cohesive surface

1. Introduction

Hard coatings on relatively soft substrates and their industrial applications have been receiving more and more attention during the past few decades. The coating industry has advanced considerably in the production of various kinds of coatings to cope with the increasing number of applications of hard-coated systems. Hard coatings are usually applied to relatively soft substrates to enhance reliability and performance. Hard ceramic coatings, for example, are used as protective layers in many mechanical applications such as cutting tools. Such coatings are usually brittle and subject to fracture of the coating or failure of the interface with the substrate. Therefore, the enhancement gained by the coatings is always accompanied by the risk of such failure.

Indentation is one of the traditional methods to quantify the mechanical properties of materials. Several techniques have been reported in the literature to extract the mechanical properties of both homogeneous

* Corresponding author. Fax: +31-50-363-4881.
E-mail address: giessen@phys.rug.nl (E. Van der Giessen).

0020-7683/02/$ - see front matter
PII: S0020-7683(01)00280-3

and composite or coated materials from indentation experiments (Bhattacharya and Nix, 1988; Doerner and Nix, 1986; Gao et al., 1992; King, 1987; Lim et al., 1999; Oliver and Pharr, 1992). Indentation has also been advocated as a tool to characterize the properties of thin films or coatings. At the same time, for example for hard wear-resistant coatings, indentation can be viewed as an elementary step of concentrated loading. For these reasons, many experimental as well as theoretical studies have been devoted to indentation of coated systems during recent years.

Contact-induced failure of coated systems has also been investigated during recent years (Abdul-Baqi and Van der Giessen, 2001a,b; Li et al., 1997; Li and Bhushan, 1998; van der Varst and de With, 2001; Malzbender et al., 2000; Wang et al., 1998). The main emphasis in such investigations has been to extract quantitative data about the coating and interfacial fracture energies and strengths. Diverse results have been obtained by different studies due to the complex nature of the problem and the different estimation procedures (van der Varst and de With, 2001). The complexity is mainly attributed to the fact that such system is a combination of at least two materials with different mechanical properties. Failure of such systems may include, for example, the plastic deformation of the substrate, the cracking of the coating or the failure of the interface. Interfacial delamination has been studied by the authors in previous work (Abdul-Baqi and Van der Giessen, 2001a,b). In the absence of coating cracking, delamination was found to occur in mode II driven by the shear stress at the interface outside the contact region during the loading stage. During the unloading stage, delamination was found to occur in mode I driven by the tensile stress at the interface in the contact region.

Coating cracking is one of the common failure events usually observed in indentation experiments. Radial or circumferential cracks might initiate from the coating surface or from the coating side of the interface and may grow into a through-thickness crack. Li et al. (1997) have proposed a method to estimate the fracture toughness from indentation tests. From the load drop or plateau caused by the first circumferential crack, they estimate a strain energy release to create the crack. The fracture energy is then calculated using the energy release, the crack area and the elastic properties of the coating. This approach has been also used by others (Li and Bhushan, 1998; van der Varst and de With, 2001; Malzbender et al., 2000). van der Varst and de With (2001) have performed Vickers indentation experiments on TiN coatings on tool steel. Arguing that the energy release which is estimated from the load–displacement curve is spent in both creating the crack and some plastic dissipation in the substrate, they estimate an upper bound of 54 J/m^2 for the fracture energy of the coating. However, the method they have used to estimate the energy release from the load–displacement curve is different from the one suggested by Li et al. (1997).

The objective of the present paper is to provide an improved understanding of coating cracking during indentation. To this end, numerical simulation of the indentation process is performed. The coating is assumed elastic and strong, the substrate is elastic-perfectly plastic and the indenter is spherical and rigid. Coating cracking is modeled by means of cohesive zones. The cohesive zone methodology allows the study of crack initiation and propagation without any separate criteria since the fracture characteristics of the material are embedded in a constitutive model for the cohesive zone. The emphasis in this study will be on circumferential cracks which initiate from the coating surface, its imprint on the load–displacement curve and the spacing between successive cracks. Using our numerical findings, the above-mentioned estimates of the fracture energy are tested. The effect of the material, geometric and cohesive parameters is also investigated.

2. Problem formulation

The system considered in this study is illustrated in Fig. 1. It comprises an elastic-perfectly plastic substrate coated by an elastic thin coating and indented by a spherical indenter. The indenter is assumed rigid and only characterized by its radius $R = 25$ μm. Assuming both coating and substrate to be isotropic,

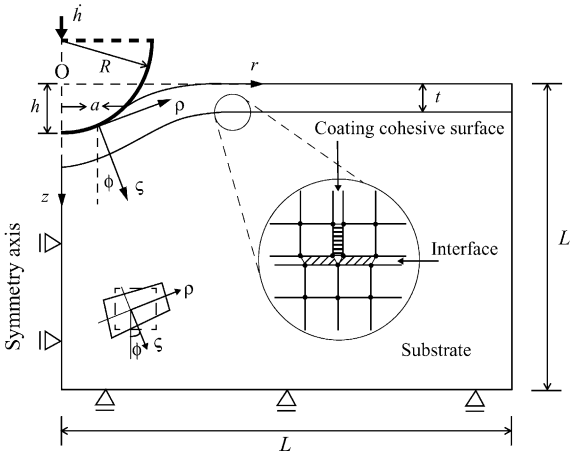

Fig. 1. Geometry of the analyzed problem, including definition of local frame of reference, (ρ,ζ), and detail of the layout of continuum elements and cohesive elements along the interface.

the problem is axisymmetric, with radial coordinate r and axial coordinate z in the indentation direction. The coating is characterized by its thickness $t = 1$ μm and elastic properties ($E_c = 500$ GPa, $\nu_c = 0.33$) and is bonded to the substrate by an interface. The substrate is supposed to be a standard isotropic elastoplastic material with plastic flow being controlled by the von Mises effective stress σ_e. It is taken to have a height $L - t$ and a radius L, with L large enough compared to film thickness so that the solution is independent of L and the substrate can be regarded as a half space; thus, it is only characterized by its elastic properties ($E_s = 200$ GPa, $\nu_s = 0.33$) and the yield stress $\sigma_y = 1.0$ GPa.

The precise boundary conditions are also illustrated in Fig. 1. The indentation process is performed incrementally with a constant indentation rate $\dot{h} = 1$ mm/s. Outside the contact area, with radius a measured in the reference configuration, the film surface is traction free,

$$t^r(r,0) = t^z(r,0) = 0 \quad \text{for } a \leqslant r \leqslant L. \tag{1}$$

Inside the contact area we assume perfect sliding conditions. The boundary conditions are specified with respect to a local frame of reference (ρ,ζ) that is rotated over an angle ϕ such that ζ is always perpendicular to the coating surface as shown in Fig. 1. The definition of this frame for points inside the material is also shown in Fig. 1. The angle ϕ is calculated for each material element in the deformed state (solid line) based on the rotation of the element with respect to its original configuration (dashed line). In the normal direction, the displacement rate $\dot{u}_\zeta$ is controlled by the motion of the indenter, while in the tangential direction the traction t^ρ is set to zero, i.e.

$$\dot{u}_\zeta(r,z) = \dot{h}\cos\phi, \quad t^\rho(r,z) = 0 \quad \text{for } 0 \leqslant r \leqslant a. \tag{2}$$

The substrate is simply supported at the bottom, so that the remaining boundary conditions read

$$u_z(r,L) = 0 \ \text{ for } 0 \leqslant r \leqslant L; \qquad u_r(0,z) = 0 \ \text{ for } 0 \leqslant z \leqslant L. \tag{3}$$

The indentation force F is computed from the tractions in the contact region,

$$F = \int_0^a t^z(r,0)2\pi r\,\mathrm{d}r. \tag{4}$$

The analysis is carried out numerically using a finite strain, finite element method. The mesh is an arrangement of four-noded quadrilateral elements. The elements are built up of four linear strain triangles

in a cross arrangement to minimize numerical problems due to plastic incompressibility. To resolve properly the high stress gradients under the indenter and for an accurate detection of the contact nodes, the mesh is made very fine locally near the contact area with an element size of $t/10$.

Since the indenter is rigid, contact nodes are identified simply by their spatial location with respect to the indenter. At a certain indentation depth h and displacement increment Δh, the node is considered to be in contact if the vertical distance between the node and the indenter is not greater than Δh. Local loss of contact may occur if an open crack falls into the contact region. In the calculations, contact is released when the nodal force becomes tensile. We have used a threshold value for tensile nodal forces equal to the average current nodal force. A value that is an order of magnitude smaller did not show any significant effect on the results. After a node is released from contact, the distance between the node and the indenter is checked each increment for possible re-formation of contact.

Coating cracking is represented by inserting cohesive zones into the coating, perpendicular to the surface. A cohesive zone is also used to model the interface between coating and substrate. A cohesive zone is a surface along which a small displacement jump between the two sides is allowed with normal and tangential components Δ_n and Δ_t, respectively. The cohesive behavior is specified in terms of a constitutive equation for the corresponding traction components T_n and T_t at the same location.

The cohesive law we adopt in this study is the one given by Xu and Needleman (1993). The traction components are determined by two potentials $\phi_n(\Delta_n, \Delta_t)$ and $\phi_t(\Delta_n, \Delta_t)$ according to

$$T_n = \frac{\partial \phi_n}{\partial \Delta_n}, \quad T_t = \frac{\partial \phi_t}{\partial \Delta_t}. \tag{5}$$

The resulting traction-separation relations in normal and tangential direction are illustrated in Fig. 2. In both directions, the peak traction represents the cohesive strength and the area under the curve corresponds to the work of fracture. The work of normal (tangential) separation, $\phi_n(\phi_t)$, can be expressed in terms of the corresponding strengths $\sigma_{max}(\tau_{max})$ as

$$\phi_n = \exp(1)\sigma_{max}\delta_n, \qquad \phi_t = \sqrt{\frac{1}{2}\exp(1)}\tau_{max}\delta_t, \tag{6}$$

where δ_n and δ_t are two characteristics lengths and $q = \phi_t/\phi_n$ is a coupling parameter. From the previous equations, the normal and tangential strengths are related by

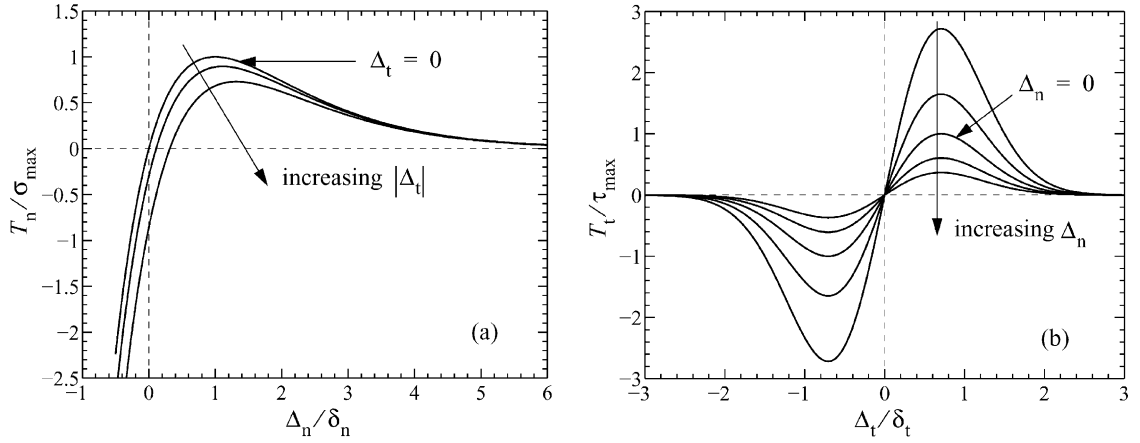

Fig. 2. The normal and shear cohesive tractions: (a) normal traction $T_n(\Delta_n)$ and (b) shear traction $T_t(\Delta_t)$. Both are normalized by their respective peak values σ_{max} and τ_{max}.

$$\sigma_{\max} = \frac{1}{q\sqrt{2\exp(1)}} \frac{\delta_t}{\delta_n} \tau_{\max}. \tag{7}$$

More details of this constitutive model are found in Xu and Needleman (1993) and Abdul-Baqi and Van der Giessen (2001a). The cohesive zones are incorporated in the finite element calculation using linear two noded elements with two Gaussian integration points which is consistent with the type of continuum elements in the coating and the substrate.

For the cohesive zones at the interface we have chosen $\delta_n = \delta_t = 0.1$ μm, $q = 0.4288$ and $\phi_n = 200$ J/m^2. Making use of Eqs. (6) and (7), these values correspond to $\sigma^i_{\max} = \tau^i_{\max} = 7.36$ GPa. For the coating $\delta_n = \delta_t = 1.0$ nm, $q = 0.4288$ and $\phi_n = 30$ J/m^2 so that $\sigma^c_{\max} = \tau^c_{\max} = 11$ GPa. The values assigned to the work of separation for both coating and interface are comparable to these obtained by Wang et al. (1998) for diamond-like carbon coatings on steel substrates. The values assigned to the characteristic lengths δ_n and δ_t for both interface and coating were chosen such that, when combined with the work of separation, reasonable values for the strength are obtained. In terms of the coating material and the cohesive parameters, the critical stress intensity factors for mode I and II fracture along a cohesive zone, i.e K_{IC} and K_{IIC}, are $(E_c\phi_n/(1-\nu_c^2))^{1/2}$ and $(E_c\phi_t/(1-\nu_c^2))^{1/2}$, respectively (Xu and Needleman, 1994). The ratio of K_{IIC} to K_{IC} being $\sqrt{q}$ is about 0.65. This value is reasonable compared to the values obtained by different experimental estimates as listed in Malzbender et al. (2000).

The effect of the variation of some of previously given parameters, such as the coating thickness, the coating Young's modulus, the yield stress and the coating cohesive parameters will be investigated. The values given in this section will serve as a reference case in this study. In the remainder of this study we will drop the superscripts from quantities referring to the cohesive parameters since, unless otherwise specified, they all will refer to the coating.

3. Stress distribution in a perfect coating

Before performing the cracking analysis, it is instructive to have a brief look at the stresses that generate in a perfect coating during indentation (i.e. without cohesive zones). Fig. 3(a) shows the radial stress distribution along the coating surface, $\sigma_{\rho\rho}(r)$. A tensile radial stress is found outside the contact area with a maximum at $r \approx 1.25a$, where a is the instantaneous contact radius. It should be noted that the location of this maximum is strongly dependent on the ratio t/R. For the same indentation depth, the smaller the ratio t/R, the closer the location of the maximum tensile stress to the contact edge. The radial stress is found to be compressive within the contact area $r < a$. It is interesting to note in Fig. 3(a) the decrease of the compressive stress in the contact region with increasing indentation depth. This is a consequence of the plastic flow of the substrate material in the indented region which induces an additional positive radial straining in the coating, leading to a decrease in the compressive stress at the contact region. Tensile stress is also seen along the coating side of the interface as shown in Fig. 3(b). It is located at the contact region $r < a$ with a maximum at the symmetry axis. This suggests that a circumferential crack is likely to initiate from the interface at $r < a$ or the coating surface at $r \approx 1.25a$ due to the maximum tensile radial stresses at these regions.

The distribution of the shear stress $\sigma_{\rho\zeta}$ along the mid-plane of the coating is shown in Fig. 3(c). The highest value of this stress is found under the contact edge at $r = a$. The shear stress has a smaller maximum value than the radial stress and furthermore is located at the edge of the contact where only relatively small tensile radial stresses are found. This indicates that shear stress is likely to play a minor role in the fracture process. Comparing the radial stresses along the surface with those on the coating side of the interface, we see that each tensile stress is faced by a compressive stress on the opposite side of the coating due to the bending-like loading. This indicates that a crack, whether initiated at the surface or the interface, will not be

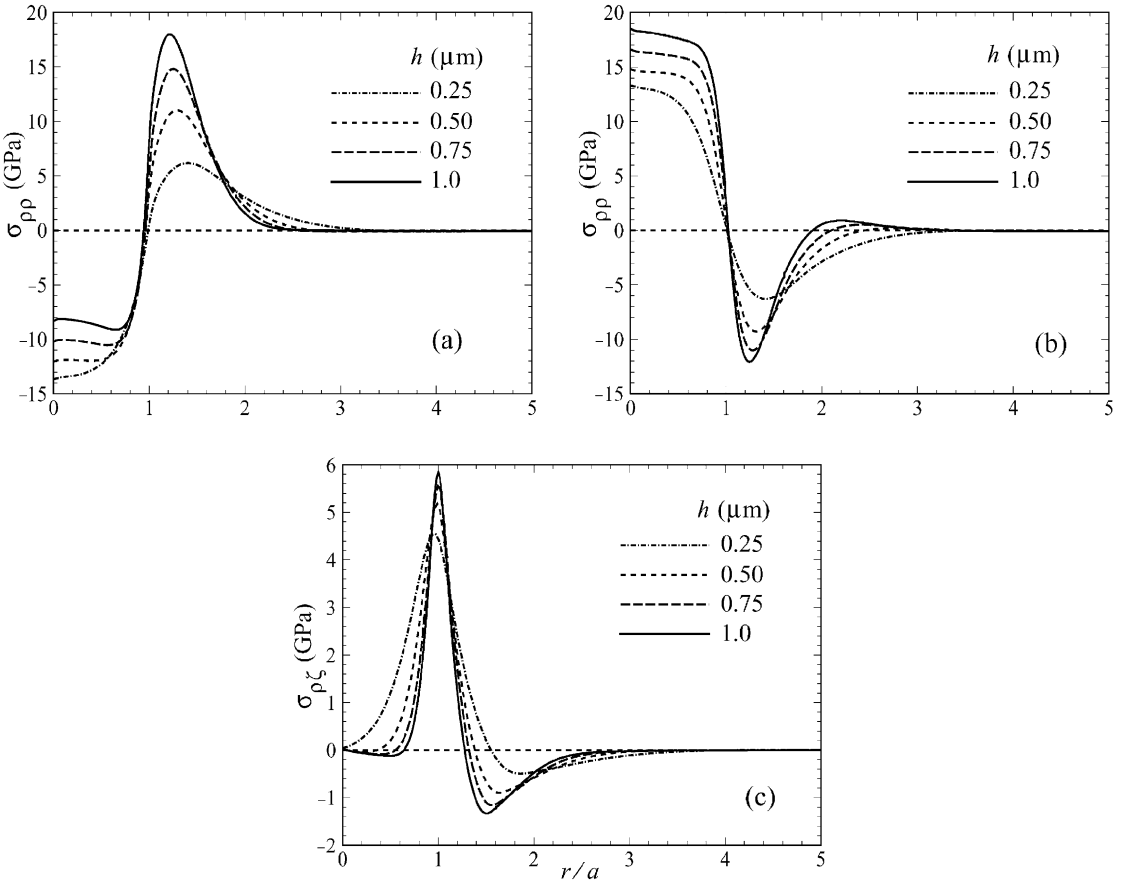

Fig. 3. Stress distribution at several indentation depths for $t/R = 1/25$: (a) radial stress along the coating surface, (b) radial stress along the coating side of the interface and (c) shear stress along the middle plane in the coating ($z = t/2$).

able to propagate through the whole coating thickness. Tensile radial stresses at the surface and interface are seen to be of the same order of magnitude. But crack initiation and propagation from the coating side of the interface suffers an extra resistance as this requires some interfacial shearing (see inset in Fig. 1) and hence more energy. Therefore, the main emphasis in this study will be on cracks that initiate from the coating surface and advance towards the interface. Cracks which initiate from the coating side of the interface do not have any significant effect on surface cracks as will be discussed later in this paper.

4. Analysis

A first approach to simulate coating failure was to place cohesive zones in between all continuum elements in the coating, as pioneered by Xu and Needleman (1993, 1994). Contrary to their work, however, the present computation is a quasi-static one and this led to serious numerical problems. The numerical problems originate from the fact that some adjacent cohesive zones reach the peak traction $\sigma_{\max}$ and start softening almost simultaneously, which breaks the uniqueness of the solution. Mesh refinement does not

solve the problem. When fine meshes are used, the region of more or less homogeneous, high tensile radial stresses comprises several elements so that there is an even larger probability of running into a loss of uniqueness. On the other hand, using coarser meshes to overcome this problem decreases the accuracy in representing the high stress gradients in the coating and the precise contact between the indenter and the coating. In addition, embedding of cohesive elements leads to an artificial enhancement of the overall compliance (Xu and Needleman, 1994). This increase will tend to underestimate the stresses in the coating and therefore the occurrence of failure. Since the compliance increase is proportional to the number of cohesive zones, we adopt a procedure in this study in which the number of cohesive zones is minimized.

The location of the necessary cohesive zones is determined in the following way. We first conduct a calculation without any cohesive zone and we trace the evolution of the maximum tensile radial stress along the coating surface along with its location at each indentation increment. This is shown in Fig. 4, with the steps in the curves originating from the node-to-node growth of the contact region. After an initial transient, both the maximum stress and its location seem to increase linearly with the contact radius a. The first crack is predicted to occur when $\sigma_{\rho\rho}^{\max} = \sigma_{\max}$. Fig. 4 shows that $\sigma_{\max} = 11$ GPa is reached when the contact radius a is 3.7 μm ($h = 0.5$ μm) and at the radial location $r = 5.0$ μm.

In the second step, a new calculation is carried out with a single cohesive zone being placed at this location prior to indentation. The first crack will then indeed form at the expected indentation depth and we continue the computation to determine the location of the second crack in the same way as for the first crack. A third computation is then started with two cohesive zones, etc. Continuing this procedure, more cracks are simulated. Fig. 5 gives the result after the fourth step in which three coating cracks have developed. Fig. 5(a) shows the distribution of radial stress $\sigma_{\rho\rho}$ at an indentation depth of 0.75 μm. The first crack at $r = 5.0$ μm is visible in the figure and a tensile stress is seen to develop in the coating outside the crack radius. At an indentation depth of $h = 1.25$ μm, three cracks have already occurred at locations 5.0, 6.4 and 7.9 μm, see Fig. 5(b). The crack at $r = 6.4$ μm is not visible in the figure since it has closed up. The first crack has also closed from the surface side as a result of the compressive stress in the contact region. Note that local loss of contact has occurred above the closed-up crack as explained in Section 2. The third crack did not reach the interface yet at this stage of loading due to the compressive stress in this region.

The procedure is further illustrated in Fig. 6(a), showing the evolution of the maximum radial stress along the coating surface. The maximum stress is seen to increase with indentation depth until the moment

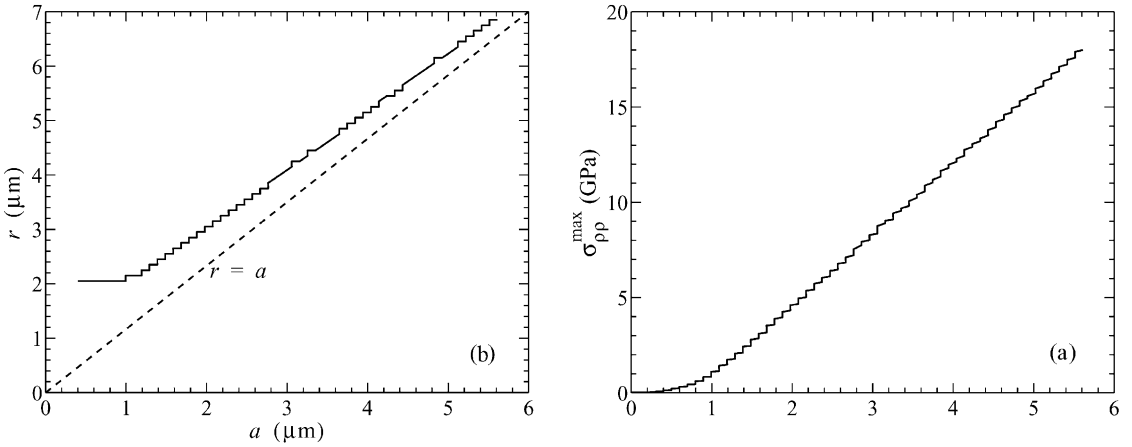

Fig. 4. (a) Evolution of the maximum radial stress at the coating surface $\sigma_{\rho\rho}^{\max}$ with the contact radius a and (b) the corresponding location r at the coating surface at which the stress is maximum.

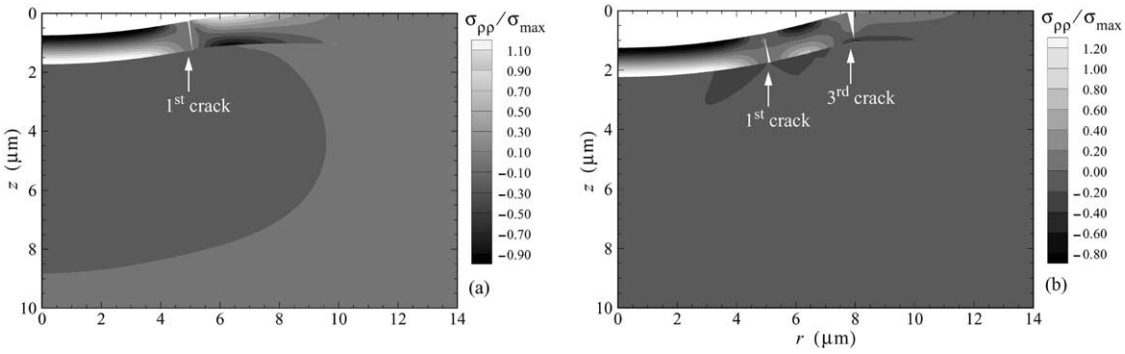

Fig. 5. Distribution of the radial stress $\sigma_{\rho\rho}$ at indentation depths of 0.75 μm (a) and 1.25 μm (b).

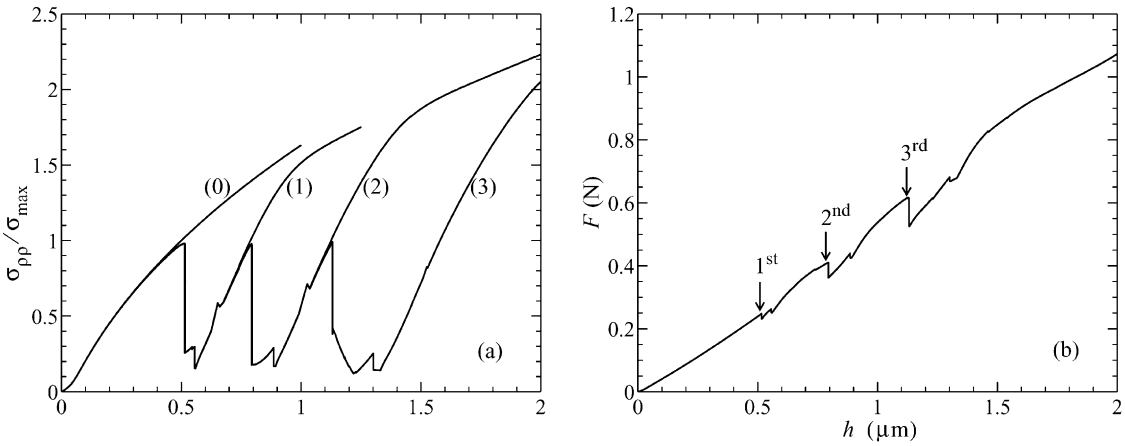

Fig. 6. (a) Evolution of the maximum radial stress at the coating surface $\sigma_{\rho\rho}^{\max}$ with the indentation depth h. The curves belong to four different calculations with the number of cohesive surfaces (and later cracks) increasing from 0 to 3. (b) Load–displacement curve for the case shown in Fig. 5. Arrows point to sudden load drops caused by cracking events.

of failure where a sudden drop occurs due to stress relaxation and redistribution. After initiation, the crack propagates through the coating thickness and stops just before reaching the interface due to the compressive stress at that region. About 10% of the coating thickness remains intact for a while until it shears off (mode II) and later opens in mode I resulting in two small drops in the maximum stress. The location of the fourth crack is predicted to be $r = 9.4$ μm after $h = 1.55$ μm. The four successive cracks thus found are seen to have an almost uniform spacing λ of 1.5 μm. The dependence of crack spacing on some of the model parameters will be discussed in Section 5.

The corresponding load–displacement curve shown in Fig. 6(b) reflects these cracking events by a sudden drop of the load. Each of three major drops on the curve is associated with the initiation of a crack. Since the fracture energy is proportional to the crack radius, the larger the crack radius, the larger the drop in the load. With further indentation, the contact radius increases, thus expanding the tensile region at the interface. The growth of the freshly nucleated crack to the interface gives rise to small load drops in between the major ones. The third crack shown in Fig. 5(b) for example reaches the interface forming a complete through-thickness crack at an indentation depth of 1.3 μm. This gives rise to the small load drop seen on the load–displacement curve at this depth.

These results demonstrate that the procedure described above is indeed capable of predicting the initiation and growth of coating cracks within the cohesive zone framework. It should be pointed out, however, that even with this small number of cohesive zones, some numerical problems were faced at first. Careful examination has shown that these were caused by the fact that the cohesive zone parameters chosen here approach atomic separation properties. The coating strength is on the order of tens of GPa's and the critical opening is only a nanometer. The consequence of this is that the cohesive stiffness beyond the peak strength is very large, and negative, which would lead to local snap back in the finite element system. This can probably be dealt with using, for instance, indirect displacement control (de Borst, 1987), but we have adopted a simpler method to circumvent this. The idea is to reduce the instantaneous stiffness of the cohesive zone as soon as the normal strength is reached, $\Delta_n \geqslant \delta_n$, but to update the tractions directly from Eq. (5). Of course, this leads to an error in the solution, but this error is corrected by way of the equilibrium correction in the next time step. Practically speaking, the effect of this procedure is that snap back instabilities are avoided and stability is maintained. Extensive testing has shown that the final error in, for example, the traction continuity between a cohesive zone element and a continuum element is smaller than a few percent, even when the instantaneous cohesive zone stiffness is reduced down to 5%.

Cracks initiating from the coating side of the interface have been excluded from the simulations despite the high tensile stress found there. The main reason is the fact that the maximum tensile stress is always found at the symmetry axis (Fig. 3b). A cohesive surface at this location will have a zero area in an axisymmetric formulation making it impossible to simulate. To study the effect of coating cracking starting from the interface, three cohesive surfaces are placed at radial locations of 1.5, 3.0 and 4.5 μm. Being all located at distances less than 5.0 μm (the expected location of the first surface crack), surface cracks are not expected to occur. The radial stress distribution at an indentation depth of 1.0 μm and the evolution of the maximum radial stress on the coating surface are shown in Fig. 7. Cracks at the three specified locations are seen to have occurred. None of these cracks has reached the surface since at the moment of initiation of each crack, the opposite side of the coating is already in contact and hence the stress state is compressive. The stress at the coating surface outside the contact region is mainly driven by the contact between the indenter and the coating at the contact edge $r = a$. Since all cracks initiating from the coating side of the interface lie in the region $r < a$, their effect on the stress outside the contact region is insignificant as shown in Fig. 7(b).

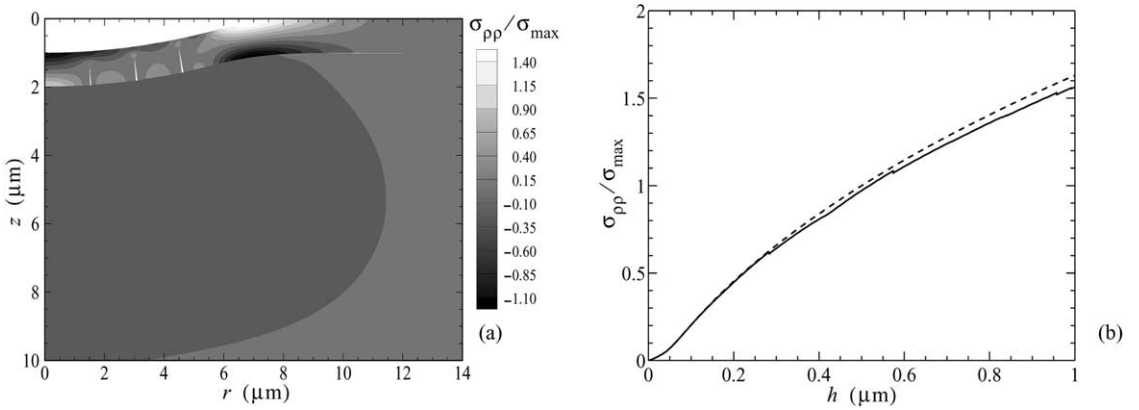

Fig. 7. (a) Distribution of the radial stress $\sigma_{\rho\rho}$ at an indentation depth of 1.0 μm. It illustrates the three cracks initiating from the coating side of the interface at locations 1.5, 3.0 and 4.5 μm. (b) The corresponding maximum radial stress at the coating surface $\sigma_{\rho\rho}^{\max}$ (solid line) compared with the stress of the noncracked coating (dashed line).

5. Effect of geometrical, material and cohesive parameters

The effect of various parameters on the initiation of the first circumferential crack and the spacing λ between successive cracks is studied. The chosen parameters are: the coating thickness t, the coating Young's modulus E_c, the substrate yield stress σ_y and the cohesive properties, i.e. coating strength σ_{max} as well as the coupling and reversibility of the cohesive tractions.

The coating thickness t and indenter radius R are the main length scales in the system and their effect is studied by varying the nondimensional parameter t/R. Fig. 8 shows the variation of the crack spacing with the coating thickness. The relation $\lambda/R \approx 1.4t/R$ provides the best linear fit. It should be noted that spacing in this figure is taken to be distance between the first two cracks. From the average spacing we get $\lambda/R \approx 1.5t/R$. In the remainder of this study, λ will refer to the average crack spacing.

Fig. 9 shows the location of the first crack as a function of the coating thickness and corresponding indentation depth for two values of σ_{max}. It can be seen that first crack occurs closer to the contact edge for

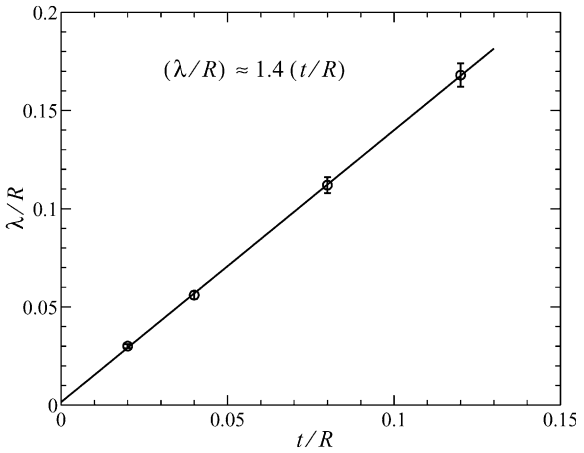

Fig. 8. Normalized crack spacing (λ/R) versus normalized coating thickness (t/R). Single points are the numerical results and solid line is a linear fit. The error in λ is $(\pm)$ half the finite-element size.

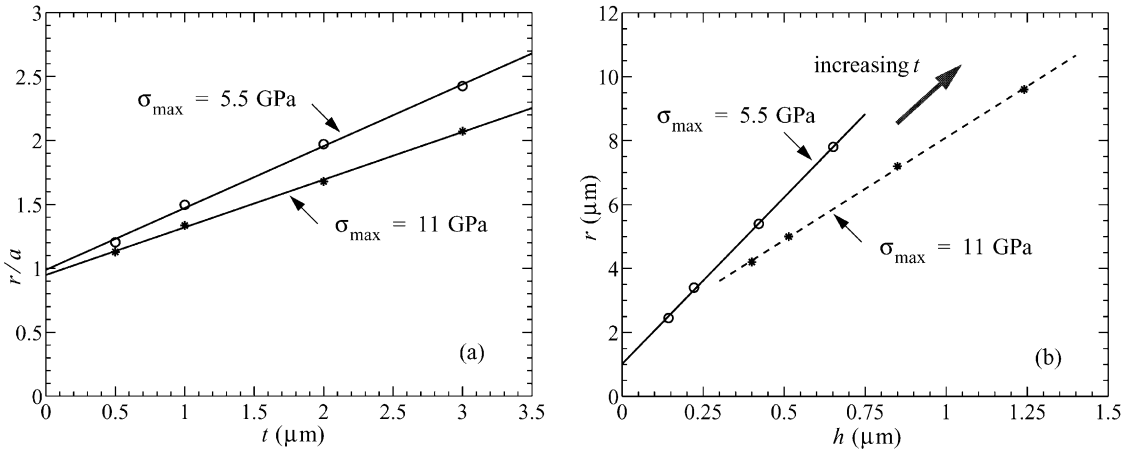

Fig. 9. The location of the first circumferential crack as a function of the coating thickness (a) and the corresponding indentation depth (b) for two values of σ_{max}. Discrete points are numerical results, lines are linear fits.

thinner coatings and higher strengths. Moreover, the thicker the coating the larger the indentation depth required to form the first crack.

A variation of the coating's Young's modulus E_c ranging from 200 to 500 GPa did not have any effect on crack spacing. However, the location of the first crack and the corresponding indentation depth strongly depend on E_c. The radial stress in the coating $\sigma_{\rho\rho}$ is proportional to the degree of bending and to Young's modulus. Therefore, coatings of lower modulus require more bending or equivalently larger indentation depths to reach the fracture strength and subsequently crack. Since the location of the maximum stress on the coating surface increases with indentation depth (Fig. 4b), coatings of lower Young's modulus crack at larger radii as seen in Fig. 10. An increase in the coating strength σ_{max} seems to be equivalent to a decrease in the Young's modulus in terms of location of the first crack and the corresponding indentation depth as shown in Fig. 10. This suggests that the first crack radius and the corresponding indentation depth depend on the ratio σ_{max}/E_c which can be considered a measure of the critical strain for cracking. Contrary to the Young's modulus, the coating strength does have some influence on crack spacing. Strengths of $\sigma_{max} = 5.5$ and 16.5 GPa resulted in crack spacings of 1.2 and 1.8 μm, respectively.

The effect of the yield stress σ_y of the substrate is studied by comparing the results obtained using three different values, namely, 0.5, 1.0 and 2.0 GPa. These values resulted in first circumferential cracks of radii of 5.6, 5.0 and 4.7 μm, respectively. The corresponding indentation depths did not deviate significantly from the reference case, where $h = 0.5$ μm. The crack spacing increased to 1.9 μm for $\sigma_y = 0.5$ GPa, whereas it decreased to 1.2 μm in the case of $\sigma_y = 2.0$ GPa. The effect of the yield stress is explained in terms of the size of the plastic zone. At the same indentation depth h, the lower the yield stress, the larger the plastic zone size. The expansion of the plastic zone towards the surface is partially accommodated by bending of the coating outside the contact region. Therefore, lower yield stresses tend to lead to larger radial location of the maximum stress on the coating surface and therefore a larger crack radius. The corresponding larger crack spacing is also explained by the same argument.

The effect of friction between the indenter and the coating on the location of the first crack and the crack spacing is also investigated. In the case of perfect sticking contact conditions, the first crack occurred at a radius $r = 5.5$ μm and a corresponding indentation depth $h = 0.59$ μm, instead of $r = 5.0$ μm and

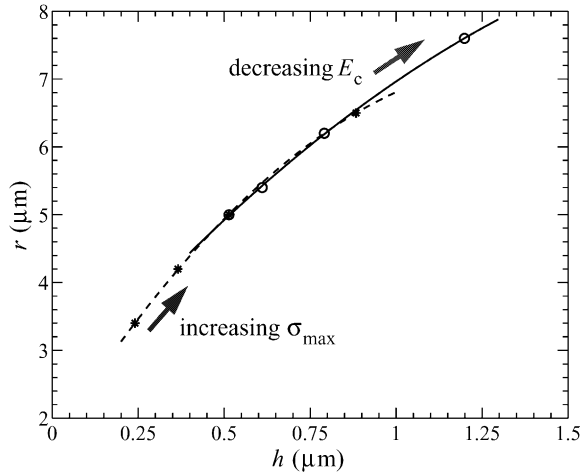

Fig. 10. The location of the first circumferential crack versus the corresponding indentation depth. Open circles are the numerical results using E_c of 200, 300, 400 and 500 GPa, $\sigma_{max} = 11$ GPa. Stars correspond to values of σ_{max} of 5.5, 8.25, 11 and 16.5 GPa, $E_c = 500$ GPa. Lines are quadratic fits.

$h = 0.5$ μm obtained previously in the case of perfect sliding contact. The crack spacing also increased from 1.5 to 2 μm when perfect sticking was assumed.

Souza et al. (2001) have experimentally investigated the spacing of indentation-induced cracks in titanium nitride coatings on stainless steel substrates. They have used a Rockwell B indenter ($R = 795$ μm) and coating thicknesses of 0.4, 2.1 and 4.2 μm. They have found that cracks are almost uniformly spaced which is consistent with our numerical results. The crack spacings observed for the various thicknesses were found to be 1.5, 5.0 and 10.0 μm, respectively, so that λ/R varies between $2.4t/R$ and $3.75t/R$. However, these experimental values are seen to be larger than those obtained in our calculations. There may be several reasons for this discrepancy. One reason is the presence of residual compressive stresses of 0.7–1.5 GPa in the coatings investigated by Souza et al. (2001), whereas in the current simulations, the coating is assumed to be stress free prior to indentation. Another reason is the friction between the indenter and the coating which is usually present in indentation experiments. In the presence friction, the crack spacing increases as mentioned previously. In addition, the material parameters chosen in this study are not precisely those of titanium nitride coatings on stainless steel substrates. Variation of these parameters has been shown above to influence the crack spacing.

The coupling and reversibility in the cohesive law are also investigated. In the original Xu-Needleman formulation (Xu and Needleman, 1993), the constitutive law of the cohesive zone is assumed to be reversible, so that the loading and unloading paths are the same. In this case, if a crack closes it heals and the system recovers all the energy consumed. Even though this energy is very small in comparison with the plastic dissipation, the effect of taking it into account is studied by using an irreversible version of the tractions. Therefore, we modify the constitutive law by introducing a secant unloading branch as illustrated in Fig. 11. If the opening velocity changes sign (unloading), the traction is assumed to decrease linearly to zero as the opening diminishes to zero (Camacho and Ortiz, 1996). The same method is applied to the shear traction. It should be noted that in the presence of coupling between the tractions, the formulation for irreversibility would not be clear. Therefore, the effect of reversibility is studied by comparing the results achieved when using reversible and irreversible uncoupled tractions. On the other hand, the effect of coupling is investigated by studying the difference between using coupled and uncoupled reversible tractions.

The results of coupled reversible tractions which has been used so far are compared to the results obtained when using uncoupled reversible tractions; i.e., $T_n = T_n(\Delta_n, \Delta_t = 0)$ and $T_t = T_t(\Delta_t, \Delta_n = 0)$ (cf.

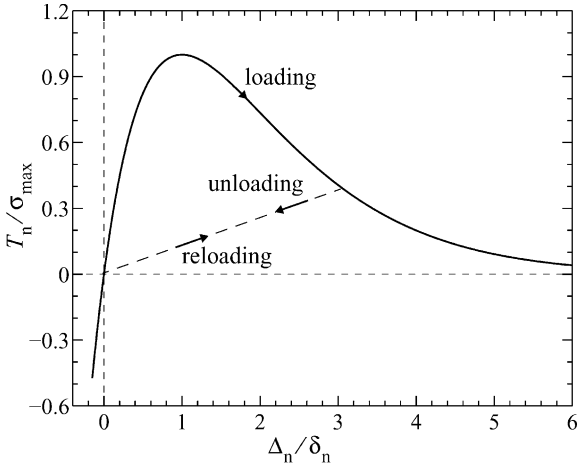

Fig. 11. Irreversible normal cohesive traction $T_n(\Delta_n)$ at $\Delta_t = 0$.

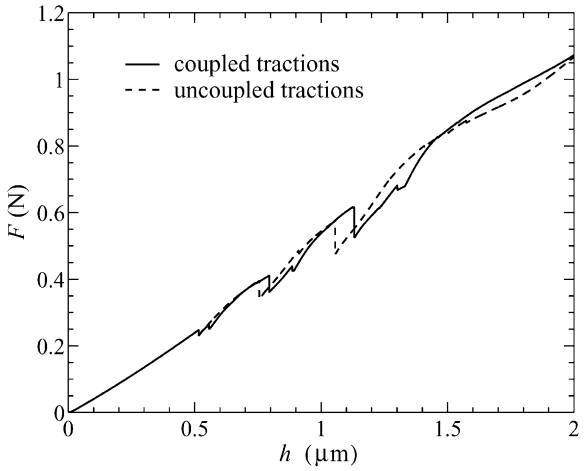

Fig. 12. Load–displacement curve for uncoupled traction-separation laws in the cohesive zones compared to the coupled ones.

Fig. 2). Three cracks were simulated and the location of the fourth one is predicted as explained in Section 4. The crack spacing is found to be 1.3 μm, which is less than the value of 1.5 μm found previously in the presence of coupling. Moreover, additional cracks occur at smaller indentation depths compared to the corresponding ones in the presence of coupling. This is demonstrated in Fig. 12. When a crack opens, the shear strength is reduced in the presence of coupling as demonstrated in Fig. 2(b). The moment the crack reaches the interface, it shears off by the shear stress which is present around the contact edge (Fig. 3c). The shearing leads to some relaxation of the coating in the form of unbending. Compared to the uncoupled tractions where shearing off does not occur, indenting to larger depth is required to arrive to the same degree of bending and form an additional crack. Moreover, larger indentation depth means that the maximum tensile stress on the coating surface occurs at a larger radius. This explains the larger crack spacing in the case of coupling. Reversibility of the tractions does not seem to have any significant effect on the results, even though we have noticed crack closure taking place (e.g. Fig. 5b). Uncoupled reversible and irreversible tractions lead to almost indistinguishable load–displacement curves and to the same crack spacing, $\lambda = 1.3$ μm.

6. Fracture energy estimates

Several researchers have tried to estimate the fracture energy from indentation experiments. One of the approaches which has been used is to estimate the energy consumed to create the first circumferential crack from the corresponding load drop or plateau on the load–displacement curve (Li et al., 1997; Li and Bhushan, 1998; van der Varst and de With, 2001; Malzbender et al., 2000). In this section we will compare the prediction of these methods with our numerical findings.

Li et al. (1997) have suggested an approach which is based on the idea that all the energy released upon the formation of a crack, ΔU, is consumed in creating the crack with fracture energy ϕ_n per unit area. By determining ΔU, the fracture energy can be estimated as

$$\phi_n^{est} = \frac{\Delta U}{2\pi r t}, \tag{8}$$

with r the crack radius and t the coating thickness. Two methods have been suggested in the literature to estimate ΔU from the load–displacement curve, as illustrated in Fig. 13. The first method (Li et al., 1997) is

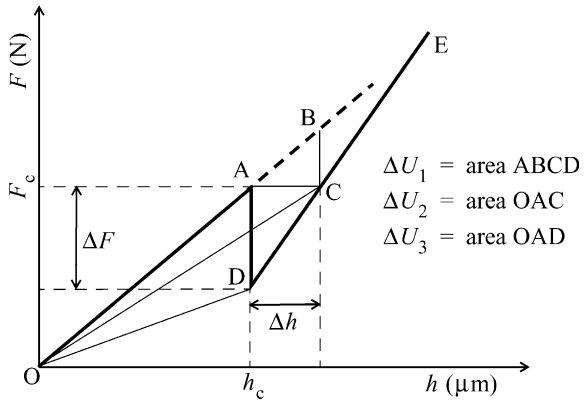

Fig. 13. Schematic load–displacement curve. ΔU_1 to ΔU_3 are different estimates of the energy release associated with a cracking event.

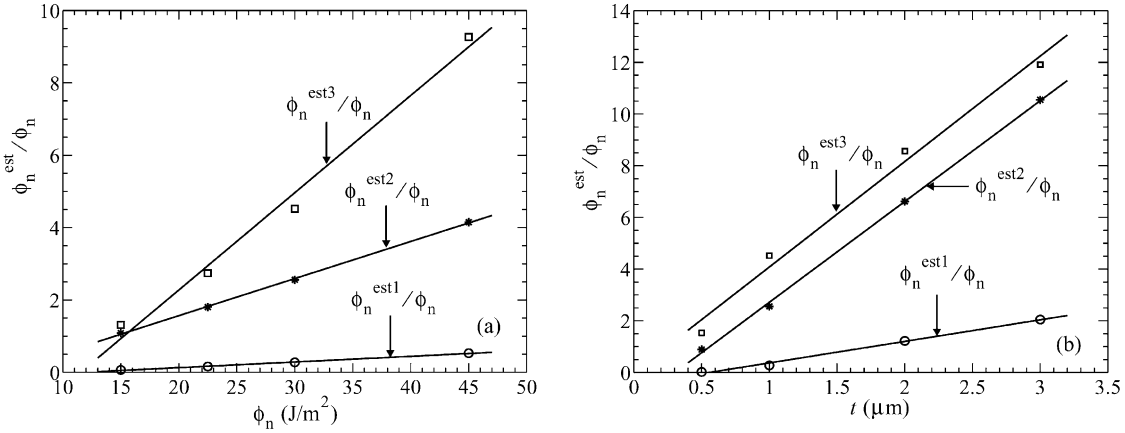

Fig. 14. Estimates for ϕ_n from Eq. (8). ϕ_n^{est1}, ϕ_n^{est2} and ϕ_n^{est3} are based on the energies ΔU_1, ΔU_2 and ΔU_3 (cf. Fig. 13), respectively. (a) Estimated values versus the actual ones for $t = 1.0$ μm. (b) Estimated values versus the coating thickness for $\phi_n = 30$ J/m^2. In (a) and (b) single points are numerical results and lines are linear fits.

to extrapolate the load in a tangential direction from the beginning to the end of the discontinuity. The difference between the areas under the extrapolated curve and the discontinuous one (ΔU_1 in Fig. 13) is taken to be the estimate of the energy release. The second method (van der Varst and de With, 2001) estimates the energy release as half the cracking load F_c times the displacement jump Δh (ΔU_2 in Fig. 13). We here suggest a third method which estimates the energy release as half the cracking indentation depth h_c times the load jump (ΔU_3 in Fig. 13). The second and third methods are borrowed from linear elastic fracture mechanics for cracking under constant load and constant displacement (indentation depth), respectively (Kanninen and Popelar, 1985).

We now use our numerical simulations to test the accuracy of the estimates obtained from Eq. (8). Obviously, the values of the energy release estimated in the three methods are completely different and so will be the estimated fracture energies. Based on our numerical results, Fig. 14 shows the estimated values of the coating fracture energy for several values of ϕ_n and t. At low values of ϕ_n or t, the first method underestimates the fracture energy, whereas the second and third methods give reasonable estimates. On the other hand, at large values of ϕ_n or t, the second and third methods overestimate the fracture energy,

whereas the estimation by the first method seems reasonable. Therefore, estimations of the coating fracture energy from indentation experiments might lead to values different from the actual ones by as much as one order of magnitude. The origin for the discrepancy is the fact that the estimates assume linearity of the problem, while in fact it is quite nonlinear because of the energy dissipation in the plastic zone in the substrate. Nevertheless, it is interesting to note the proportionality between the normalized estimated values and the actual ones and the coating thickness.

7. Concluding remarks

In this paper, cracking of hard coatings on elastic-perfectly plastic substrates during indentation has been studied using the finite element method. Cracking of the coating was simulated by assuming single or multiple planes of potential cracks across the coating thickness at pre-determined radial locations prior to indentation. These planes are assigned a finite strength and modeled by means of cohesive zones. The interface between the coating and the substrate was also modeled by means of cohesive zones but with interface properties.

The emphasis was on circumferential cracks which initiate from the coating surface outside the contact edge and advance towards the interface. The initiation and advance of such cracks is imprinted on the load–displacement curve as a sudden load drop (kink). The larger the crack radius, the larger the load drop, since the energy released by the crack is proportional to the crack area. After initiation, the crack advances almost spontaneously across the coating thickness and stops just before reaching the interface as a result of a compressive stress at that side. With further indentation, the tensile region under the indenter expands and when it encompasses the crack tip, the crack advances until the interface creating a complete through-thickness crack. This is also imprinted on the load–displacement curve by a relatively smaller load drop. For several coating thicknesses, the ratio of the crack radius to the instantaneous contact radius was found to increase linearly with the coating thickness. The smaller the coating thickness, the closer this ratio is to unity.

With further indentation, successive cracking occurs at larger radii, which each additional crack also imprinted on the load–displacement curve as a kink. The crack spacing was found to be predominantly controlled by the ratio of the coating thickness to the indenter radius. For a fixed indenter radius, the crack spacing is of the order of the coating thickness. Variation of the coating Young's modulus did not show any influence on crack spacing, whereas spacing increased with the coating strength and decreased with the substrate yield stress. Coupling and irreversibility of the cohesive tractions were also investigated. The presence of coupling was found to slightly increase crack spacing. Moreover, additional cracking occurs at higher indentation depths compared to uncoupled tractions. Reversible and irreversible cohesive tractions have led to almost indistinguishable results in terms of crack spacing and load–displacement data. The predicted crack spacings are consistent with those obtained in recent experiments by Souza et al. (2001).

Finally, it has been shown that estimation of the coating fracture energy from the first crack area and corresponding load drop, as commonly done in indentation experiments, leads to values different from the actual ones by as much as one order of magnitude. The reason for this is that a small portion of the energy release is consumed by the crack, while the rest of the energy is consumed by the accompanied plastic dissipation in the substrate.

References

Abdul-Baqi, A., Van der Giessen, E., 2001a. Indentation-induced interface delamination of a strong film on a ductile substrate. Thin Solid Films 381, 143–154.

Abdul-Baqi, A., Van der Giessen, E., 2001b. Delamination of a strong film from a ductile substrate during indentation unloading. J. Mater. Res. 16, 1396–1407.

Bhattacharya, A.K., Nix, W.D., 1988. Analysis of elastic and plastic deformation associated with indentation testing of thin films on substrates. Int. J. Solids Struct. 24, 1287–1298.

Camacho, G.T., Ortiz, M., 1996. Computational modelling of impact damage in brittle materials. Int. J. Solids Struct. 33, 2899–2938.

de Borst, R., 1987. Computation of post-bifurcation and post-failure behaviour of strain-softening solids. Comput. Struct. 25, 211–224.

Doerner, M., Nix, W., 1986. A method for interpreting the data from depth-sensing indentation instruments. J. Mater. Res. 1, 601–609.

Gao, H., Chiu, C.-H., Lee, J., 1992. Elastic contact versus indentation modeling of multi-layered materials. Int. J. Solids Struct. 29, 2471–2492.

Kanninen, M.F., Popelar, C.H., 1985. Advanced Fracture Mechanics. Oxford University Press, New York.

King, R.B., 1987. Elastic analysis of some punch problems for a layered medium. Int. J. Solids Struct. 23, 1657–1664.

Li, X., Bhushan, B., 1998. Measurement of fracture toughness of ultra-thin amorphous carbon films. Thin Solid Films 315, 214–221.

Li, X., Diao, D., Bhushan, B., 1997. Fracture mechanisms of thin amorphous carbon films in nanoindentation. Acta Mater. 45, 4453–4461.

Lim, Y.Y., Chaudhri, M.M., Enomoto, Y., 1999. Accurate determination of the mechanical properties of thin aluminum films deposited on sapphire flats using nanoindentations. J. Mater. Res. 14, 2314–2327.

Malzbender, J., de With, G., den Toonder, J.M.J., 2000. Elastic modulus, indentation pressure and fracture toughness of hybrid coatings on glass. Thin Solid Films 366, 139–149.

Oliver, W.C., Pharr, G.M., 1992. An improved technique for determining hardness and elastic modulus using load and displacement sensing indentation experiments. J. Mater. Res. 7, 1564–1583.

Souza, R.M., Sinatora, A., Mustoe, G.G.W., Moore, J.J., 2001. Numerical and experimental study of the circular cracks observed at the contact edges of the indentations of coated systems with soft substrates. Wear 251, 1337–1346.

van der Varst, P.G.Th., de With, G., 2001. Energy base approach to the failure of brittle coatings on metallic substrates. Thin Solid Films 384, 85–89.

Wang, J.S., Sugimura, Y., Evans, A.G., Tredway, W.K., 1998. The mechanical performance of DLC films on steel substrate. Thin Solid Films 325, 163–174.

Xu, X.-P., Needleman, A., 1993. Void nucleation by inclusion debonding in a crystal matrix. Model. Simul. Mater. Sci. Eng. 1, 111–132.

Xu, X.-P., Needleman, A., 1994. Numerical simulations of fast crack growth in brittle solids. J. Mech. Phys. Solids 42, 1397–1434.